

MULTI-OBJECTIVE OPTIMIZATION OF HOT BLAST STOVE HEAT EXCHANGER

热风炉换热器多目标优化

Ye ZHANG¹⁾; Qing JIANG^{*1,2)}; Liangyuan XU^{1,2)}; Chao HUANG¹⁾; Huasheng GAN¹⁾¹⁾ College of Engineering, Anhui Agricultural University, Anhui/China²⁾ Anhui Province Engineering Laboratory of Intelligent Agricultural Machinery and Equipment, Anhui/China

Tel: +86_0551-65786450; E-mail: jtao@ahau.edu.cn

Corresponding authors: Qing Jang

DOI: <https://doi.org/10.35633/inmateh-69-23>

Keywords: Heat exchanger, Hot-blast stove, Multi-objective genetic algorithm, Numerical simulation, Response surface method

ABSTRACT

Shell-and-tube heat exchangers are widely used in many research fields and industrial production processes, but little research has been conducted on the use of heat exchangers for drying crops. This study conducted a numerical simulation of the temperature, velocity, and pressure fields based on the shell-and-tube fluids of a heat exchanger in a biomass particle hot-blast stove. The correctness of the simulation results was verified by test data before simulation, and the mesh was verified to be irrelevant. The application of a multi-objective genetic algorithm in heat exchanger design and optimization was explored, considering five design variables, such as hot tube diameter, transverse pitch, longitudinal pitch, cold flow velocity, and hot flow velocity for optimization. The Nusselt number, friction factor, and comprehensive performance coefficient were used as objective functions for 2D and 3D response surface analysis. The final design variables $P1=74.91$ mm, $P2=104.23$ mm, $P3=121.37$ mm, $P4=4.83$ m/s, and $P5=8.48$ m/s were obtained to improve the comprehensive performance coefficient by 16.11%. The heat transfer performance was improved by 9.55% and the resistance performance was reduced by 15%.

摘要

管壳式热交换器在许多研究领域和工业生产过程中被广泛使用,但对热交换器用于干燥农作物的研究却很少。本研究对生物质颗粒热风炉中基于壳管式流体的热交换器的温度、速度和压力场进行了数值模拟。仿真前通过测试数据验证了仿真结果的正确性,并验证了网格的无关性。探讨了多目标遗传算法在换热器设计和优化中的应用,考虑了热管直径、横向间距、纵向间距、冷流速、热流速等五个设计变量进行优化。以努塞尔数、摩擦系数和综合性能系数作为目标函数进行二维和三维响应面分析。最终得到的设计变量 $P1=74.91$ mm, $P2=104.23$ mm, $P3=121.37$ mm, $P4=4.83$ m/s, $P5=8.48$ m/s, 综合性能系数提高了 16.11%。传热性能提高了 9.55%, 阻力性能降低了 15%。

INTRODUCTION

Despite the global shortage of energy, most traditional drying devices are coal fired. As an alternative, biomass pellet hot-air stoves are energy-saving and environmentally friendly drying devices that provide a heat source for drying crops. These furnaces are fueled by renewable energy sources such as plants (including algae, wood chips, and crops) and organic substances such as livestock manure, with improved combustion conditions (Wickramaarachchi and Narayana, 2020; McKendry, 2002). The parts comprising these furnaces include a heat exchanger, combustion chamber, and blower. The role of the heat exchanger is to transfer heat from the hot fluid to the cold fluid device, and its performance directly affects the applicability and reliability of the biomass pellet hot-air furnace. Many experimental and numerical methods have been proposed to obtain the natural-convection heat transfer and fluid flow characteristics of shell-and-tube tube heat exchangers.

Numerical simulations and computer techniques are increasingly used by scholars to analyze and solve a multifaceted range of drying problems. Numerical simulation has developed relatively quickly in China and has evolved from being used to validating models to solving practical problems, which requires a rigorous combination of theory with practice (Jiang et al., 2021).

¹ Ye Zhang, M.S. Stud. Eng.; Qing Jiang, Prof. M.S. Eng.; Liangyuan Xu, Prof. Ph.D. Eng.; Chao Huang, M.S. Stud. Eng.; Huasheng Gan M.S. Stud. Eng.

As for the structure of a heat exchanger, to improve performance to reduce the drop in the pressure of the shell-side fluid, scholars have investigated the thermal performance of tie round tubes, embedded ties, spiral ties, spiral bellows, and spiral folded plates at different shell velocity (Guo *et al.*, 2011; Liu *et al.*, 2015; Tan *et al.*, 2012; Sharifi *et al.*, 2018; Dong *et al.*, 2015). In addition, some scholars have studied the effect of different heat exchanger tube diameters and different baffle sizes on the thermal performance of heat exchangers at different shell velocity (Chen *et al.*, 2016; Xie *et al.*, 2019; Naqvi *et al.*, 2019; Shahril *et al.*, 2017), and other scholars have studied the effect of different fluid materials on heat exchanger performance. Sheikholeslami *et al.*, (2015), studied the fluid flow and heat transfer in an air–water double tube heat exchanger, and Heydari *et al.*, (2018), used numerical simulations to study how the addition of different nanoparticles to the fluid affects the performance of a folded plate shell and tube heat exchanger. Kim and Cho (2018) analyzed the airside heat transfer and pressure drop of louver-finned parallel flow heat exchanger. In summary, many scholars have formulated schemes to improve heat exchanger performance in terms of structure, dimensions, and fluid materials—achieving great breakthroughs in numerical simulations, whether in China or abroad. However, the final goal of these studies was to improve heat exchanger performance.

Thus, in this study, the boundary conditions were calculated for a heat exchanger according to the design requirements of a biomass pellet hot-blast furnace. Ansys Fluent software was used to perform numerical simulations of two-phase flow heat transfer, and the structural and flow parameters of the heat exchanger were optimized with multi-objective optimization methods (Kamiyama *et al.*, 2022; Tharakeshwar *et al.*, 2017; Mirzaei *et al.*, 2017; Raja *et al.*, 2017a, 2017b; Gu *et al.*, 2019). The optimal parameters under different operating conditions were summarized by response surface analysis, and the adequacy was analyzed to prove the reliability of the results; the sensitivity was analyzed to determine the weights of the design variables on the output parameters. For single-objective optimization problems, it is difficult to weigh the contradictions of multiple objective functions, whereas multi-objective optimization methods can solve such problems. This method enables simultaneous optimization of multiple variables, with a high degree of continuity in optimization, and provides good predictability and intuition for heat exchanger design, which ultimately leads to optimal design parameters.

MATERIALS AND METHODS

Establishment of heat exchanger model

The focus of the research was on heat exchangers in biomass particle hot-blast furnaces. In this study, the heat exchanger was composed of four tube processes and one shell process. The gas in the tube side was a high-temperature flue gas produced through combustion in a biomass pellet furnace, and the air in the shell side was at room temperature. High-temperature air is obtained through heat exchange in a hot tube, and at a certain temperature, the air enters the dryer to dry the grain. The total length of the heat exchanger was 1,900 mm, the total width was 610 mm, the total height was 1,540 mm, and the tube diameter of the heat exchanger tube was 76 mm. The computational domain in this paper consists of a solid domain and two fluid domains (air domain and flue gas domain) as shown in Fig. 1. The simplified model of heat exchanger is mainly consisted of shell, heat transfer tube bundle and baffle plate.

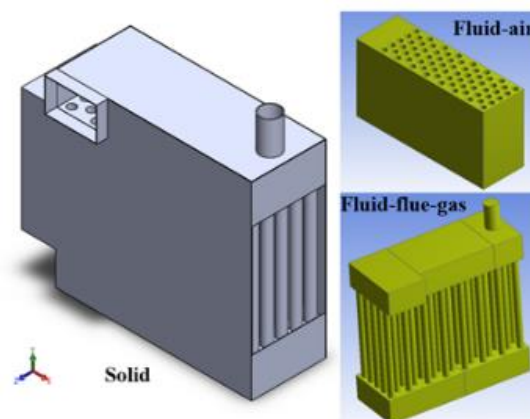


Fig. 1 - Simplified heat exchanger model

Setting materials and boundary conditions

The heat exchanger of the biomass pellet hot-blast stove was made of Q235 steel, when analyzing the flow field of the heat exchanger model, the material properties of the air and high-temperature flue gas should be fully considered. The materials were defined through the Fluent software, and the specific material parameters (Zhang et al., 2009) are presented in Table 1.

Table 1

Material characteristics set				
Materials	Density (kg/m ³)	Specific Heat [J/(kg-K)]	Thermal conductivity [W/(m-K)]	Viscosity (m ² /s)
Steel	7850	502	48.6	
Air	1.205	1005	0.0259	1.81×10 ⁻⁵
Flue gas	0.363	1239	0.0827	4.07×10 ⁻⁵

According to the design requirements, 200,000 kcal of heat is generated per hour:

$$W = Q_{out} = 200000 \text{ kcal} / h = 232.60 \text{ kW} \tag{1}$$

Because of the design of the hot-air stove, the thermal efficiency cannot reach 100%. Due to the thermal resistance between the solid wall of the heat exchanger and the fluid, and the heat loss from the environment was considered. Thus, a 20% heat transfer loss was therefore considered:

$$Q_{in} = W \times (1 - 20\%) = 186.08 \text{ kW} \tag{2}$$

$$Q_{in} = C_{air} m_{air} \Delta t_1 \tag{3}$$

$$Q_{out} = C_{fume} m_{fume} \Delta t_2 \tag{4}$$

$$m_{air} = \rho_{air} v_{air} A_{in} \tag{5}$$

$$m_{fume} = \rho_{fume} v_{fume} A_{out} \tag{6}$$

$$D = \frac{4S}{L} \tag{7}$$

where:

Q_{in} , Q_{out} is the heat absorbed by air per hour and the heat emitted by the flue gas per hour, (kW). C_{air} , C_{fume} is the average specific heat capacity of air and the average specific heat capacity of flue gas, [kJ/(kg/K)]. m_{air} , m_{fume} is the mass flow of air and the mass velocity of flue gas, (kg/s). Δt_1 , Δt_2 is the air temperature difference and the flue gas temperature difference, (°C). ρ_{air} , ρ_{fume} is the average density of air and the average density of flue gas, (kg/m³). v_{air} , v_{fume} is the air velocity and the flue gas velocity, (m/s). A_{in} , A_{out} is the air inlet area and the flue gas inlet area, (m²). D is the hydraulic diameter, (m). S is the effective area of total flow, (m²), and L is the wet circumference, (m).

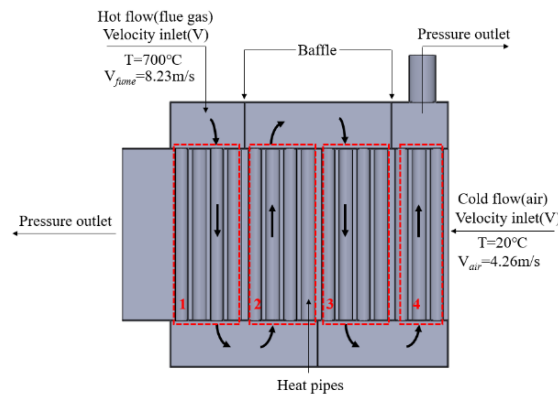


Fig. 2 - Heat exchanger boundary condition profile

The air inlet is calculated using a normal air temperature of 20°C. However, according to the design requirements of the hot-air outlet, the temperature must reach 80°C. The temperature difference is therefore 60°C. If the average specific heat of the air is 1.007 kJ/(kg/K), the density of the imported 20°C air is 1.205 kg/m³, and the air inlet cross-sectional area is 0.6 m², using equations (1), (3), and (5), the air inlet velocity is approximately 4.26 m/s.

During the heat exchange between the flue gas and air, the temperature of the flue gas changes with time. According to the test experience, the temperature of the flue gas produced by the combustion of biomass particles can reach 700°C. According to the design requirements, to make full use of the heat generated by the high-temperature flue gas, the flue gas outlet temperature must be below 100°C. The temperature difference is therefore 600°C. If the average specific heat is 1.1535 kJ/(kg/K), the density of the 700°C flue gas is 0.363 kg/m³, and the flue gas inlet cross-sectional area is 0.1125m², using equations (2), (4), and (6), the flue gas inlet velocity is approximately 8.23 m/s.

The hydraulic diameter is a common physical quantity used when dealing with flow in non-circular pipes and is defined as four times the ratio of the total flow effective area to the perimeter. It is necessary to calculate the hydraulic diameter because of the setting requirement during the simulation. According to equation (7), the hydraulic diameter of the air velocity inlet can be calculated as 0.75 m and the hydraulic diameter of the flue gas velocity inlet is 0.3263 m. The boundary condition profiles are indicated in Fig. 2.

Method for evaluating the heat transfer performance of the heat exchanger

Researchers continually strive to improve heat exchange with less power consumption, and numerous evaluation indexes to assess the performance of heat exchangers have been proposed. The main parameters evaluated are Nusselt number, pressure drop, heat transfer factor, friction factor, etc. The standard for measuring heat exchangers investigates heat transfer and resistance performance. The balance between the two has attracted much attention. The heat transfer factor and friction factor comparison method was proposed by Kays and London (1984).

In this paper, the optimized output parameters: the heat transfer performance is evaluated by the Nusselt number Nu , the resistance performance by the friction factor f , and the comprehensive performance by Pec , which are denoted by P6, P7, and P8, respectively.

$$Nu = \frac{hD}{k} \quad (8)$$

$$f = \frac{\Delta p(2D/L_0)}{\rho v^2} \quad (9)$$

$$Pec = \frac{Nu}{f^{1/3}} \quad (10)$$

where: h is the convective heat transfer coefficient, D is the hydraulic diameter, k is the thermal conductivity of fluids, ρ is the fluid density, v is the fluid inlet velocity, Δp is the differential pressure between the fluid inlet and outlet within the unit, and L_0 is the heat exchanger tube length (1m).

The convective heat transfer coefficient:

$$h = \frac{Q}{A\Delta t_m} \quad (11)$$

where: Q is the heat flux of fluid, A is the heat transfer area, Δt_m is the logarithmic mean temperature difference.

RESULTS

Grid independence verification

Fluent meshing is a powerful and highly robust mesh generation software with high-quality tetrahedral mesh and hexahedral core mesh generation algorithms. To get the grid-independent results, different cell sizes were set and the mesh models with 390W, 261W, 197W and 128W grid cells were obtained.

Setting the same boundary parameters, the shell-side outlet temperature and the pressure drop are obtained as shown in Table 2.

Table 2

Result of grid-independence

Grid number/(W)	Pressure drop/(Pa)	Relative error/(%)	Outlet temperature(°C)	Relative error/(%)
390	372.12	—	88.71	—
261	377.55	1.46	88.33	0.43
197	386.73	3.93	87.53	1.33
128	419.62	12.76	90.04	1.50

It can be found from Table 2 that the relative error of the grid model with a grid number of 261w is the lowest at 1.46% and 0.43%. It indicated that the difference between the calculation results of the two grid models was small, which reduced the number of grids by about 130W and shortened the calculation time. Therefore, the final heat exchanger was calculated using the 261W cell grid model.

The accuracy of the simulation was verified, the air outlet temperature was monitored, and the outlet temperature reached stability at about 300 steps (Fig. 3) and 88°C. This temperature deviates slightly from the calculated value of 80°C obtained under ideal conditions but meets the design requirements; thus, the simulation results are credible.

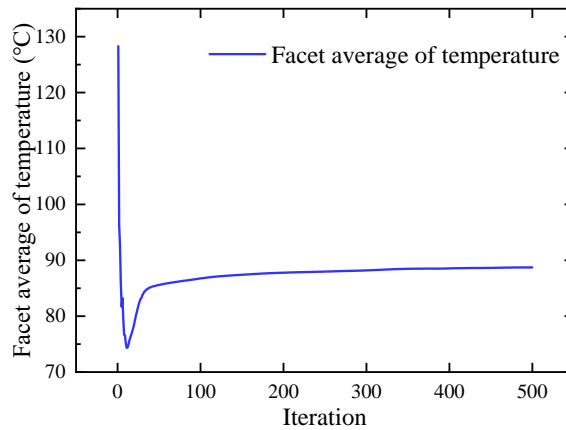


Fig. 3 - Variation of air outlet temperature with the iteration

Verification of numerical simulation correctness

In order to verify the correctness of the numerical simulation, the temperature variation of the hot air stove from ignition to hot air outlet temperature stabilization in 60 min was collected during the test of the hot air stove product as shown in Fig. 4.

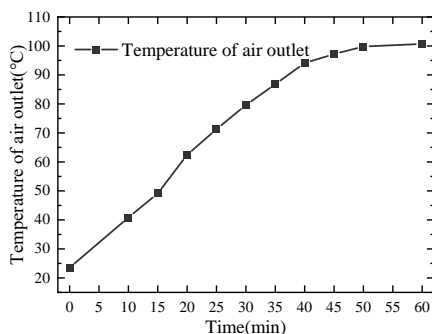


Fig. 4 - Variation of air outlet temperature with time



Fig. 5 - Biomass pellet hot air stove test device

The biomass pellet hot air stove test device is shown in Fig. 5. The temperature was measured every 5 min during the machine operation. The temperature was stabilized at about 100°C after 50 min of machine operation, and the temperature at 60 min was 100.7°C. The cold flow rate under this test condition is 4.5m/s, the ambient temperature is 23°C, and the hot flow rate is 7.8m/s. The simulation of this test condition results in an outlet temperature of 90.67°C. The difference between the simulation result and the test result under this condition is about 10.03°C, and the error is about 9.96%. The temperature difference of simulation result is 70.67°C in this condition, and the temperature difference of test is 77.7°C, and the error of both is 9.05%. Although there are some errors between the simulation results and the experimental results, these differences are attributed to the simplification of the model and the unavoidable measurement errors, which are also within the error tolerance. In the simplification of the heat exchanger model, the features irrelevant to the simulation will be reasonably deleted, simplified as follows: 1. Hot blast stove in the process of combustion, the ash cleaning port is closed, so the ash cleaning port at the bottom of the heat exchanger will be simplified. 2. The connection of the hot tubes will appear welded seams, the impact of the weld is ignored. 3. The bottom of the hot blast stove is connected by the channel steel, this paper analyzes the heat exchanger flow field, so the impact of the bottom channel steel is ignored. It is necessary to ensure the accuracy of the measurement, and high-precision sensors should be used to reduce the instrument error.

Numerical simulation results of the shell side

After modeling, meshing, determining the solution model, and defining the boundary conditions, the model was imported into a computational fluid dynamics program to obtain a numerical solution. The distribution of the temperature, air velocity, and pressure field inside the tube and shell side of the heat exchanger were obtained, and the accurate temperature distribution required for the finite element structural analysis was obtained for fluid mechanics and heat transfer. The temperature, velocity, and pressure field distribution in the middle section of the heat exchanger shell ($Y = 0$ mm) is presented in Fig. 6.

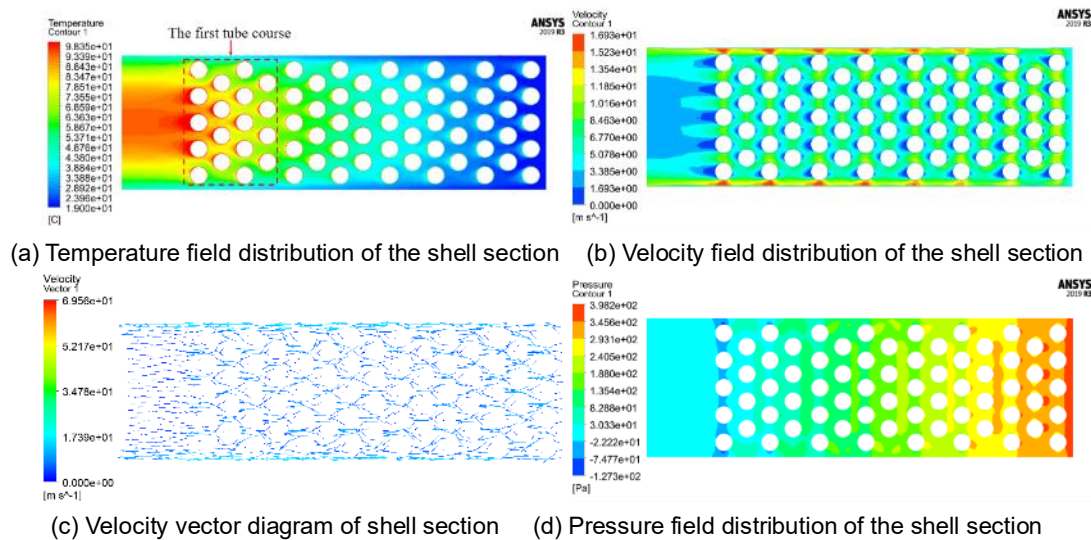


Fig. 6 - The result of shell side simulation

The clouds for the distribution of the cross-sectional temperature of the heat exchanger shell at $Y = 0$ mm are illustrated in Fig. 6(a). The change in the temperature of the shell side was large; the temperature of shell-side fluid increased after absorbing heat along the direction of fluid flow; and room-temperature air rushed toward the heat exchanger tube wall surface from the inlet to the outlet, which lowered the temperature inside the heat exchanger tube while initiating the process of heat exchange with the high-temperature flue gas. The lowest temperature at the inlet end of the heat exchanger was approximately 20°C , which was the boundary temperature set before the heat exchanger calculation, whereas the highest temperature at the outlet end reached approximately 98°C and the high-temperature region was concentrated on the first tube section. The average surface temperature at the outlet was calculated to be approximately 88°C in Fluent software. The end product was high-temperature air of 80°C , indicating that the product met the design requirements under the speed conditions.

The cross-sectional velocity of the heat exchanger shell at $Y = 0$ mm and the distribution clouds of the velocity vectors are presented in Fig. 6(b) and (c). Due to the obstruction of the heat exchanger tube when the air flowed through the heat exchanger tube bundle, the air on either side of the heat exchanger tube entered the narrow space between the two heat exchanger tubes separately. Because of the rapid decrease in flow space, the velocity of air in this narrow channel then suddenly increased. At the back of each heat exchanger tube, the speed value was low and the degree of thermal mixing was therefore small, resulting in poor local heat transfer and the formation of a flow "dead zone." In this zone, the heat exchanger heat transfer area could not be fully utilized; thus, the heat transfer coefficient and heat transfer efficiency decreased and this area was easy to scale.

The distribution cloud of the cross-sectional pressure of the heat exchanger shell side at $Y = 0$ mm is presented in Fig. 6(d). Air flowed in the shell side of the heat exchanger, and the effect of the blockage on the heat exchanger tube bundle became increasingly obvious, gradually decreasing the shell side pressure. From the perspective of the Bernoulli equation (equation 12), the total energy of the inlet section is equal to the total energy of the outlet section, which includes pressure potential energy, position potential energy, and kinetic energy. In the same section, the position potential energy is equal, and the loss of pressure reflects the change of kinetic energy at the inlet and outlet.

$$P_1 + \frac{1}{2} \rho v_1^2 + \rho g h_1 = P_2 + \frac{1}{2} \rho v_2^2 + \rho g h_2 \quad (12)$$

where: P_1, P_2 is the inlet and outlet pressure, h_1, h_2 is the position height.

Numerical simulation results of the tube side

The temperature, velocity, and pressure field distribution in the middle section of the heat exchanger tube side ($Z = 0$ mm) is illustrated in Fig. 7.

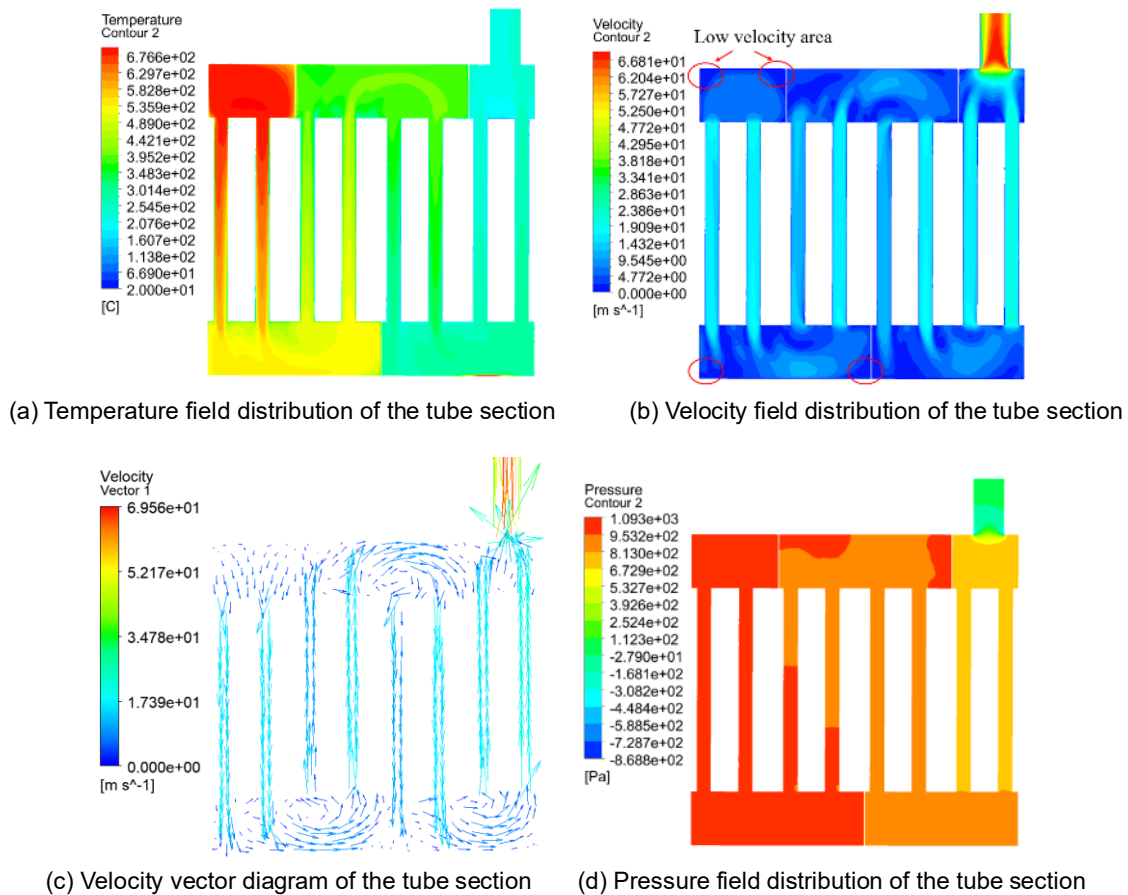


Fig. 7 - The result of tube side simulation

Fig. 7(a) presents the distribution of the temperature of the heat exchanger tube in the section at $Z = 0$ mm. The high-temperature flue gas moved in the flow direction, and the temperature differences in the different tube side were clearly observable. When the high-temperature flue gas was in the narrow flow channel, the heat transfer through the wall of the heat exchanger tube could increase the shell side air temperature. In the $Z = 0$ mm cross-section of the first, second, third, and fourth tubes, the temperatures were 676°C and approximately 400°C , 300°C , and 160°C , respectively.

The velocity and the distribution of the velocity vectors of the heat exchanger tube in the $Z = 0$ mm section are illustrated in Fig. 7(b) and (c). The distribution of the tube range velocity was relatively uniform, and the velocity above the heat exchanger tube was less than the velocity inside the tube. This was because the cross-sectional area decreased when the high-temperature flue gas entered the heat exchanger tube, thus increasing the velocity of the tube. There are low-velocity areas at the corners of the heat exchanger, which are dead angles of the flow, which leads to uneven velocity field distribution. This was because the flue gas rotated and could not flow out. These areas can accumulate dust. Therefore, a switch-type door plate should be added above this area in the structure design, which makes it easy to clean to prevent the heat exchanger tube from becoming blocked. An ash cleaning port should be installed below the heat exchanger tube to allow the furnace ash in the flue gas to be regularly removed to extend the service life of the equipment, reducing the impact of dirt on product performance and improving the product's efficiency. Fig. 7(c) depicts the heat exchanger tube side with high-temperature flue gas flowing from the fourth tube to the outlet, reaching its maximum flow at the outlet.

Fig. 7(d) presents the pressure distribution in the $Z = 0$ mm section of the heat exchanger tube, the pressure decreases gradually from the first to the fourth tube section. The overall pressure of the tube side is larger than that on the shell side. This was because the tube-side fluid velocity was greater than the shell-side fluid velocity, which resulted in the tube-side pressure being greater than the shell-side pressure.

Multi-objective optimization of shell and tube heat exchangers

The project input parameters include three structural dimensional design variables (hot tube diameter, transverse pitch, and longitudinal pitch) and two boundary parameter design variables (cold flow and hot flow velocity), denoted by P1, P2, P3, P4, and P5, respectively. In addition, the horizontal spacing between the circle centers of two hot tubes is defined as the transverse pitch; the vertical spacing between the circle centers of two hot tubes of the same centerline is defined as the longitudinal pitch. The diagram of the structure of the tube bundle arrangement is shown in Fig.8. In the optimization process, the number of hot tubes is 68 and the three parameters a, b, and c are constant values of 62 mm, 62 mm, and 342 mm, respectively. The variation of transverse pitch and longitudinal pitch will change the overall length and width of the heat exchanger but not the overall shape. The range of values of the design variables is shown in Table 3.

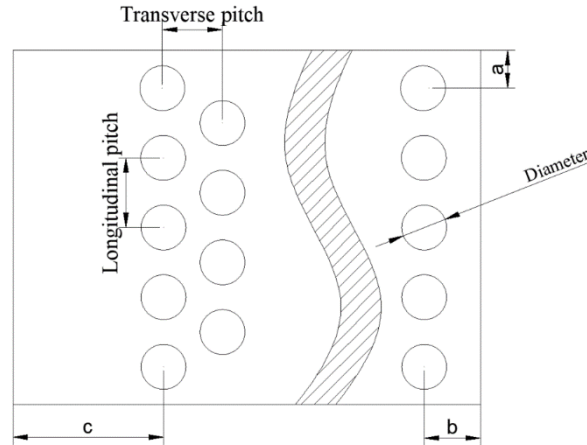


Fig. 8 - The diagram of tube bundle structure

Table 3

Range of variation of design parameters

Limit	Design Variables				
	P1/(mm)	P2/(mm)	P3/(mm)	P4/(m/s)	P5/(m/s)
Initial Value	76	102	118	4.26	8.23
Lower limit	70	90	100	2	3
Upper limit	80	112	130	6	9

The project output parameters are Nu , friction factor f , and Pec , which are expressed by P6, P7, and P8, respectively. Because the final export temperature of the product needs to reach 80°C, the final decision target is shown in Equation 13.

$$\begin{cases} \max Nu \\ \min f \\ \max Pec \\ t \geq 80 \end{cases} \quad (13)$$

In the Design of Experiment (DOE) setup for multi-objective optimization, the optimization space-filling design method with high filling capacity and low response surface error was selected, the number of samples was 40 groups, and the response surface type was set as a non-parametric regression type. The multi-objective genetic algorithm (MOGA) was selected in the final optimization combination, with 5000 response surface sample points, 1000 iteration samples, 70% maximum allowable Pareto percentage, and 20 maximum iterations.

Influence of optimization parameters on Nusselt number

After the design variables of the optimization model were confirmed, the range of variables was determined and the multi-objective optimization experimental design was completed. The first obtained is the influence between the design variables P1-P5 on the Nusselt number. The three-dimensional response surface variation of Nusselt number with hot tube diameter, transverse pitch, longitudinal pitch, cold flow velocity, and hot flow velocity is shown in Fig. 9. The input parameters that do not participate in the response in each figure take default values: P1 = 76 mm, P2 = 102 mm, P3 = 118 mm, P4 = 4.26 m/s, P5 = 8.23 m/s.

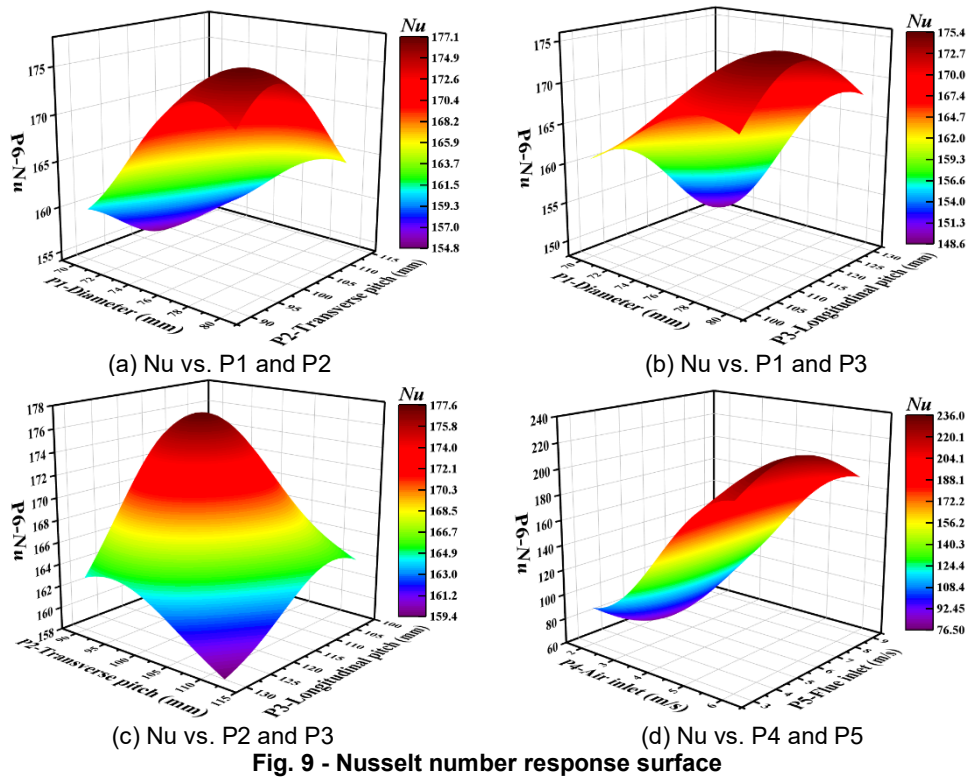
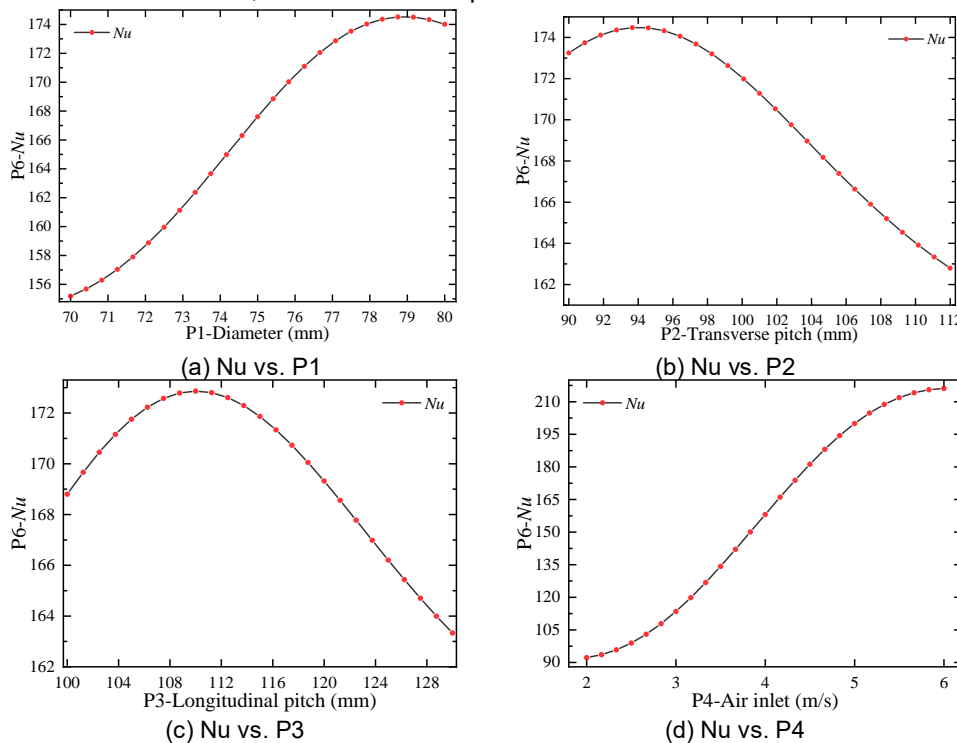


Figure 9(a) shows the response surface of the Nusselt number when the hot tube diameter and transverse pitch work together. When the hot tube diameter is between 70 and 80 mm, the Nusselt number increases and then decreases with increasing transverse pitch; when the transverse pitch is between 90 and 112 mm, the Nusselt number increases and then decreases with increasing hot tube diameter. When $P1 = 78.33$ mm and $P2 = 95.50$ mm, the maximum response value of Nusselt number is 177.07. It can be found in Fig. 9(b) that when the hot tube diameter is between 70 and 80 mm, the Nusselt number increases and then decreases with increasing longitudinal pitch. When $P1 = 78.75$ mm and $P3 = 112.50$ mm, the maximum response value of Nusselt number is 175.40. It can be found from Fig. 9(c) that the maximum response value of Nusselt number up to 177.55 when $P2 = 93.67$ mm and $P3 = 110$ mm. It can be found from Fig. 9(d) that when $P4 = 6$ m/s and $P5 = 5.5$ m/s, the maximum response value of Nusselt number is 235.71.



The influence of the one-factor design variables on the two-dimensional response curves for the Nusselt number is shown in Fig. 10. As it can be found in Fig. 10. The Nusselt number tends to increase overall with the increase of heat pipe diameter and air velocity, and the peak Nusselt number is 174.36 when $P1 = 78.33$ mm. The heat exchange area is appropriately increased, so the heat dissipation per unit time will increase, thus increasing the convective heat transfer coefficient h and making the Nusselt number larger. When $P2 = 94.58$ mm and $P3 = 111.25$ mm the Nusselt number reached the maximum value of 174.48 and 172.86 respectively.

Influence of optimization parameters on friction factor

The next obtained is the influence of design variables P1-P5 on the friction factor of the heat exchanger, the influence of two factors of the design variables on the friction factor was analyzed separately. The three-dimensional response surface variation of friction factor with hot tube diameter, transverse pitch, longitudinal pitch, cold flow velocity, and hot flow velocity is shown in Fig. 11. The input parameters that do not participate in the response in each figure take default values.

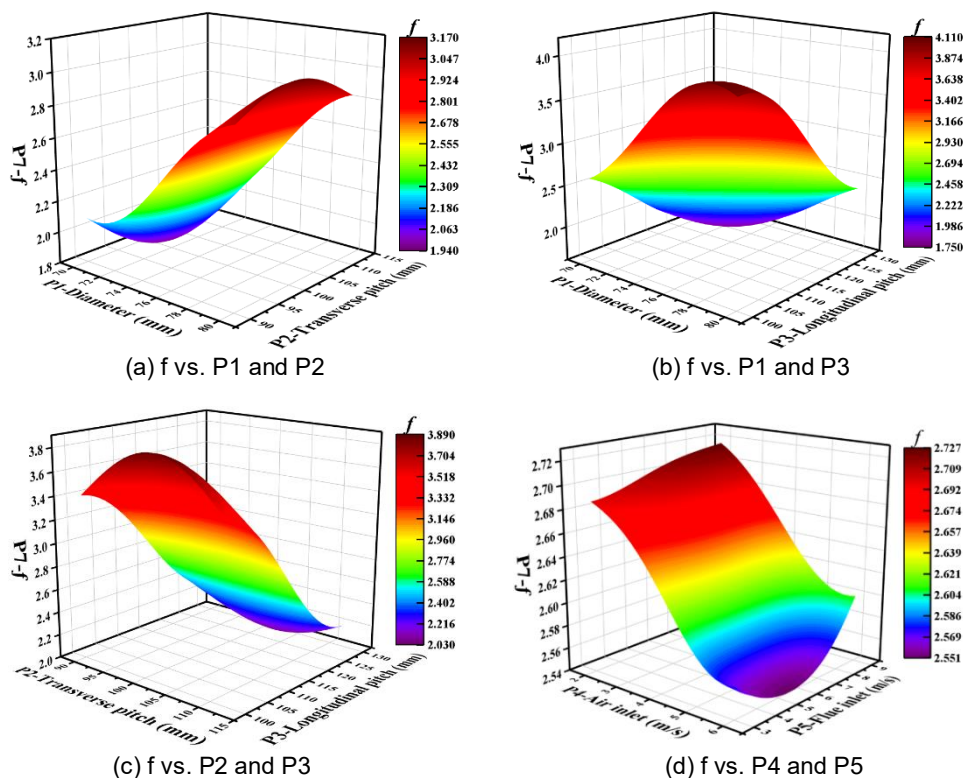


Fig. 11 - Friction factor response surface

Figure 11(a) shows the response surface of the friction factor when the hot tube diameter and transverse pitch work together. It can be found from Fig. 11(a) that the friction factor shows a trend of increasing and then decreasing with increasing hot tube diameter and transverse pitch. The minimum response value of the friction factor is 1.94 when $P1 = 70.83$ mm and $P2 = 101.92$ mm. It can be found from Fig. 11(b) that the minimum response value of the friction factor is 1.75 when $P1 = 72.08$ mm and $P3 = 126.25$ mm. It can be found from Fig. 11(c) that the minimum response value of the friction factor is 2.03 when $P2 = 102.83$ mm and $P3 = 130$ mm. It can be found from Fig. 11(d) that the minimum response value of the friction factor is 2.55 when $P4 = 5.67$ m/s and $P5 = 5.25$ m/s.

The influence of the one-factor design variables on the two-dimensional response curves for the friction factor is shown in Fig. 12. Based on the two-dimensional response curve in Fig. 12(a), it can be found that the friction factor is proportional to the hot tube diameter, which is because the increase of the diameter in a certain space increased the heat transfer area, decreased the airflow area and increased the resistance. On the contrary, it can be found from Fig. 12(b-d) that the friction factor decreases with increasing transverse pitch, longitudinal pitch, and air flow rate. This is because the increase of transverse pitch and longitudinal pitch increases the airflow area and the resistance gradually decreases.

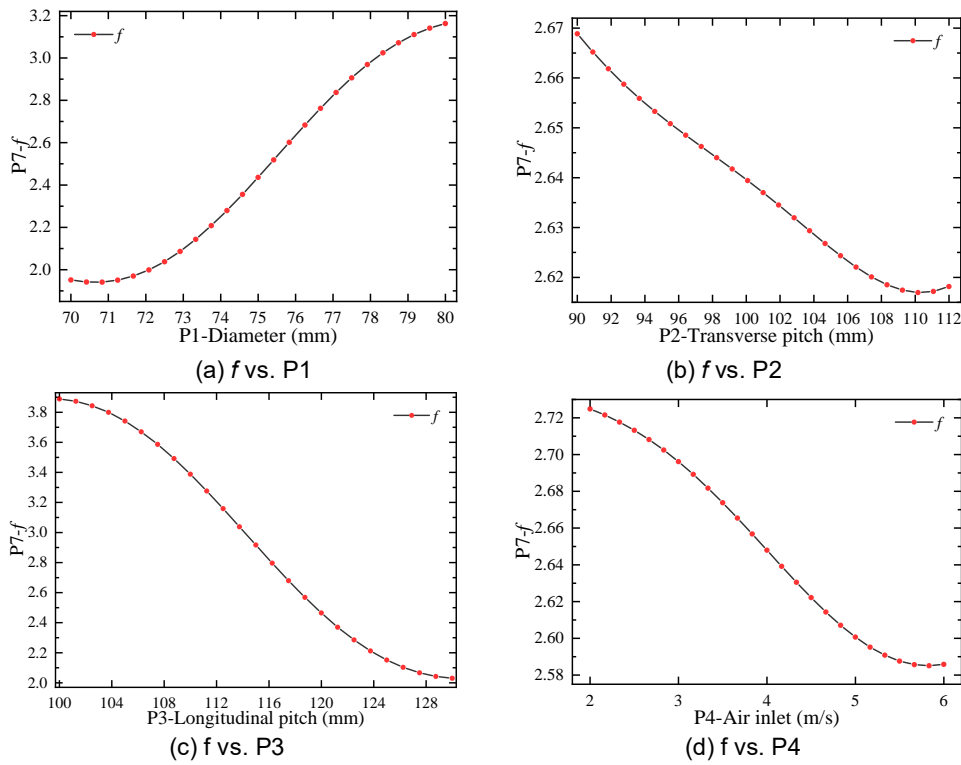


Fig. 12 - Friction factor 2D response curves

Influence of optimization parameters on comprehensive performance coefficient

The last obtained is the influence of the design variables P1-P5 on the comprehensive performance coefficient of the heat exchanger. The three-dimensional response surface variation of comprehensive performance coefficient with hot tube diameter, transverse pitch, longitudinal pitch, cold flow velocity, and hot flow velocity is shown in Fig. 13.

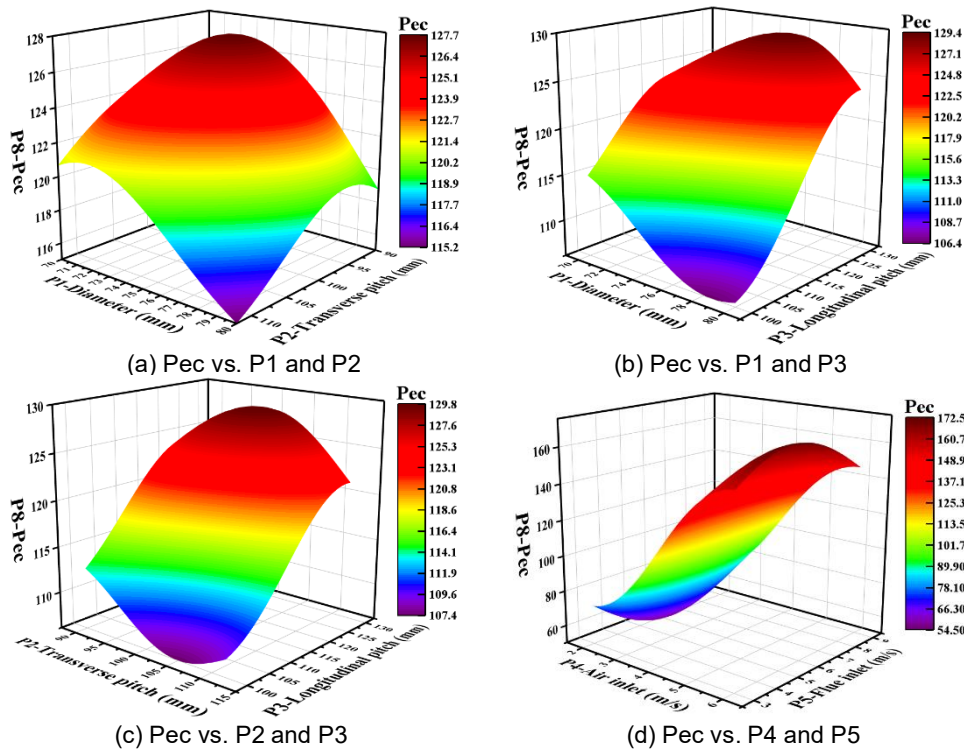


Fig. 13 - Comprehensive performance coefficient response surface

Figure 13(a) shows the response surface of the comprehensive performance coefficient when the hot tube diameter and transverse pitch work together.

It can be found from Fig. 13(a) that the maximum response value of the comprehensive performance coefficient is 127.60 when $P1 = 73.75$ mm and $P2 = 96.42$ mm. As shown in Fig. 13(b), the maximum response value of the comprehensive performance coefficient is 129.35 when $P1 = 75.42$ mm and $P3 = 127.50$ mm. It can be found in Fig. 13(c) that the maximum response value of the comprehensive performance coefficient is 129.74 when $P2 = 99.17$ mm and $P3 = 127.50$ mm. Figure 13(d) shows the response surface of the comprehensive performance coefficient when the boundary parameters air flow rate and flue gas flow rate work together. The maximum response value of the comprehensive performance coefficient is 172.35 when $P4 = 5.83$ m/s and $P5 = 5.75$ m/s.

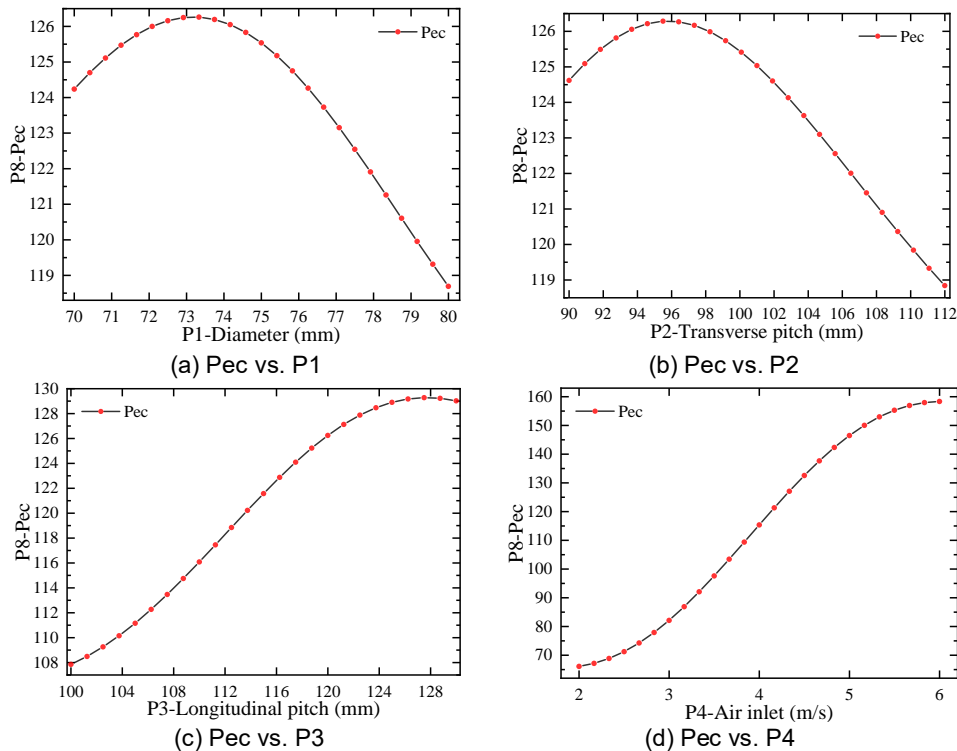


Fig. 14 - Comprehensive performance coefficient 2D response curves

The influence of the one-factor design variables on the two-dimensional response curves for the comprehensive performance coefficient is shown in Fig. 14. Based on the two-dimensional response curves in Fig. 14(a) and Fig. 14(b), it can be found that there is a peak in the effect of hot tube diameter and transverse pitch on the comprehensive performance coefficient. The comprehensive performance is best around this point, and above or below this value will have a bad effect on the performance of the heat exchanger. When $P1 = 73.33$ mm and $P2 = 95.50$ mm, the maximum response values of the comprehensive performance coefficient are 126.26 and 126.29, respectively. Figure 14(c) and Figure 14(d) show the two-dimensional response curves of the comprehensive performance coefficient with the longitudinal pitch and air flow rate, and the comprehensive performance coefficient increases with the increase of the longitudinal pitch and air flow rate.

Adequacy analysis

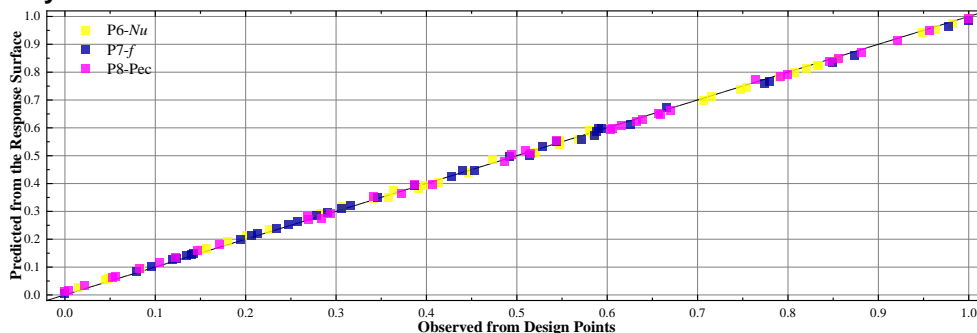


Fig. 15 - Adequacy of output parameters

After the optimization is completed, the fit can be used to determine whether the response surface predicted value fits the test value accurately. The figure of adequacy is shown in Fig. 15, the horizontal axis is

the standardized value of the observed value from the design point, and the vertical axis is the standardized value of the predicted value from the response surface. The discrete points in the figure represent the ratio between the response surface predicted value and the observed value at the design point, and the closer the discrete points are to the diagonal line, the better the response surface predicted point fits the test point. It can be seen from Fig. 15 that the fit points of the three output parameters obtained from the response surface prediction are close to the diagonal line, which further illustrates the accuracy of the simulation.

Optimization parameter sensitivity analysis

The local sensitivity reflects the closeness of the relationship between the output parameters and the input parameters. The larger the local sensitivity, the stronger the effect of the input parameters on the output parameters. Take the sensitivity of the Nusselt number as an example (equation 14):

$$Sensitivity = \frac{Nu_{max} - Nu_{min}}{Nu_{ave}} \tag{14}$$

If the input parameter is positively correlated with the output parameter, it means that the output parameter increases with the increase of the input parameter and the local sensitivity is positive. If the input parameter is negatively correlated with the output parameter, it means that the output parameter decreases with the increase of the input parameter and the local sensitivity is negative.

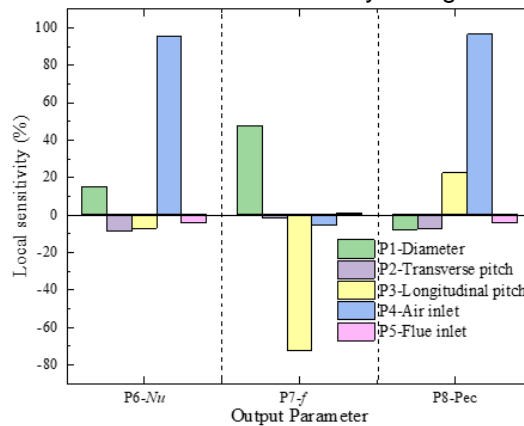


Fig. 16 - Local sensitivity of output parameters

The sensitivity of each input parameter to the output parameter is shown in Fig. 16. Air velocity and longitudinal pitch perform the most significant influence on the overall performance, followed by hot tube diameter, transverse pitch, and flue gas velocity. An increase in air velocity is beneficial for comprehensive performance. The influence of air velocity on heat transfer performance is the largest and is positively correlated; the influence of longitudinal pitch on resistance performance is the largest and is negatively correlated. A simulation result is needed to confirm an optimal value.

Optimization results

After the response surface of the heat exchanger was completed, and the accuracy of the response surface prediction was demonstrated by the fit. Based on the DOE simulation results, three sets of relatively optimal solutions were screened out as shown in Table 4.

Table 4

Results of multi-objective optimization								
Plan	P1/(mm)	P2/(mm)	P3/(mm)	P4/(m/s)	P5/(m/s)	Nu	f	Pec
Initial	76	102	118	4.26	8.23	167.96	2.60	122.15
1	74.91	104.23	121.37	4.83	8.48	184.00	2.21	141.83
2	74.30	99.83	123.98	4.66	8.83	175.20	2.05	137.76
3	75.67	101.76	119.86	4.67	7.92	187.39	2.39	140.85

It can be found from Table 4 by comparing the performance parameters with the initial structure that the Nu of schemes 1-3 increased by 9.55%, 4.31%, and 11.57%, respectively, and f decreased by 15%, 21.15%, and 8.08%, and Pec increased by 16.11%, 12.78%, and 15.31%. According to the equation of Pec, the Nusselt number of all three structures is increased and the friction factor is decreased after optimization, thus the Pec is increased. In this study, the maximum value of Pec increase was adopted as the best design point: P1=74.91 mm, P2=104.23 mm, P3=121.37 mm, P4=4.83 m/s, and P5=8.48 m/s.

Table 5

Design point verification results and optimization results

Plan	<i>Nu</i> optimized results	<i>Nu</i> validated results	<i>Nu</i> error (%)	<i>f</i> optimized results	<i>f</i> validated results	<i>f</i> error (%)	<i>Pec</i> optimized results	<i>Pec</i> validated results	<i>Pec</i> error (%)
1	184.00	180.36	1.98	2.21	2.27	2.71	141.83	137.27	3.22
2	175.20	172.14	1.75	2.05	2.10	2.44	137.76	134.38	2.45
3	187.39	179.93	3.98	2.39	2.45	2.51	140.85	133.54	5.19

In order to analyze the reliability of the optimization results, the three optimization results were reinserted as design points in the DOE scheme for simulation validation again. The validation results are shown in Table 5. It can be found from Table 5 that the maximum error between the optimization results and the validation results is 5.19%. Therefore, the accuracy of the genetic algorithm calculation was proved, and the optimization of the heat exchanger structure can be completed by the ANSYS response surface module.

CONCLUSIONS

(1) According to the calculated boundary conditions, when the simulated air velocity is 4.26 m/s and flue gas velocity is 8.23 m/s, the outlet temperature obtained is 88°C, which is higher than the product design requirement of 80°C. The numerical simulation results agree well with the calculation results, with a maximum deviation of 10%, and the results can be considered reliable.

(2) The structural parameters and flow parameters are considered. The results of single-factor and multi-factor analyses of input parameters by 2D and 3D response surfaces show that the influence of multiple input parameters is more complex and correlated with each other. Response surface optimization provides a novel method for optimizing shell and tube heat exchangers.

(3) Within the range of input parameters selected in this study, air velocity and longitudinal pitch most affect the comprehensive performance, followed by hot tube diameter, transverse pitch, and flue gas velocity. The multi-objective optimization of the heat exchanger by genetic algorithm finally determined the best design points in this study as P1=74.91 mm, P2=104.23 mm, P3=121.37 mm, P4=4.83 m/s, and P5=8.48 m/s. The comprehensive performance is improved by 16.11%.

ACKNOWLEDGEMENTS

The authors thank Fund Project: Anhui Province Science and Technology Major Special Project and Anhui Province Engineering Laboratory of Intelligent Agricultural Machinery and Equipment and Anhui Agricultural University for their funding support.

REFERENCES

- [1] Chen, H. T., Lin, Y. S., Chen, P. C., & Chang, J. R. (2016), Numerical and experimental study of natural convection heat transfer characteristics for vertical plate fin and tube heat exchangers with various tube diameters. *International Journal of Heat and Mass Transfer*, 100, 320-331. England. <https://doi.org/10.1016/j.ijheatmasstransfer.2016.04.039>
- [2] Dong, C., Chen, Y., & Wu, J. (2015). Comparison of heat transfer performances of helix baffled heat exchangers with different baffle configurations. *Chinese Journal of Chemical Engineering*, 23(1), 255-261. China <https://doi.org/10.1016/j.cjche.2014.10.014>
- [3] Gu, X., Wang, T., Chen, W., Luo, Y., & Tao, Z. (2019). Multi-objective optimization on structural parameters of torsional flow heat exchanger. *Applied Thermal Engineering*, 161, 113831. England <https://doi.org/10.1016/j.applthermaleng.2019.113831>
- [4] Guo, J., Fan, A., Zhang, X., & Liu, W. (2011). A numerical study on heat transfer and friction factor characteristics of laminar flow in a circular tube fitted with center-cleared twisted tape. *International Journal of Thermal Sciences*, 50(7), 1263-1270. France. <https://doi.org/10.1016/j.ijthermalsci.2011.02.010>
- [5] Heydari, A., Shateri, M., Sanjari, S. (2018). Numerical analysis of a small size baffled shell-and-tube heat exchanger using different nano-fluids. *Heat Transfer Engineering*, 39(2), 141-153. USA. <https://doi.org/10.1080/01457632.2017.1288052>
- [6] Jiang, Q., Zhang, Y., Yan, S., & Xu, L. (2021). Optimal Design of an Angular Box for a Mixed Flow Grain Dryer. *Applied Engineering in Agriculture*, 37(4), 555-562. USA. <https://doi.org/10.13031/aea.14643>

- [7] Kamiyama, A., Inokuma, K., Murata, A., Yamamoto, S., Iwamoto, K., & Konno, T. (2022). Multi-objective optimization of multi-stage heat sink of electric aircraft using three-dimensional thermal network analysis. *Journal of Thermal Science and Technology*, 17(1), 21-00421. Japan. <https://doi.org/10.1299/jtst.21-00421>
- [8] Kays, W. M., & London, A. L., (1984) *Compact heat exchangers*, New York: McGraw-Hill Book Company.
- [9] Kim, N. H., & Cho, H. (2018). Airside heat transfer and pressure drop of louver-finned parallel flow heat exchanger having a drainage channel. *Journal of Thermal Science and Technology*, 13(1), JTST0018-JTST0018. Japan. <https://doi.org/10.1299/jtst.2018jtst0018>
- [10] Liu, J. J., Liu, Z. C., & Liu, W. (2015). 3D numerical study on shell side heat transfer and flow characteristics of rod-baffle heat exchangers with spirally corrugated tubes. *International journal of thermal sciences*, 89, 34-42. France. <https://doi.org/10.1016/j.ijthermalsci.2014.10.011>
- [11] McKendry, P. (2002). Energy production from biomass (part 1): overview of biomass. *Bioresource technology*, 83(1), 37-46. Netherlands. [https://doi.org/10.1016/S0960-8524\(01\)00118-3](https://doi.org/10.1016/S0960-8524(01)00118-3)
- [12] Mirzaei, M., Hajabdollahi, H., & Fadaakar, H. (2017). Multi-objective optimization of shell-and-tube heat exchanger by constructal theory. *Applied Thermal Engineering*, 125, 9-19. England. <https://doi.org/10.1016/j.applthermaleng.2017.06.137>
- [13] Naqvi, S. M. A., & Wang, Q. (2019). Numerical comparison of thermohydraulic performance and fluid-induced vibrations for STHXs with segmental, helical, and novel clamping antivibration baffles. *Energies*, 12(3), 540. Switzerland. <https://doi.org/10.3390/en12030540>
- [14] Raja, B. D., Jhala, R. L., & Patel, V. (2017). Many-objective optimization of cross-flow plate-fin heat exchanger. *International Journal of Thermal Sciences*, 118, 320-339. France. <https://doi.org/10.1016/j.ijthermalsci.2017.05.005>
- [15] Raja, B. D., Jhala, R. L., & Patel, V. (2017). Many-objective optimization of shell and tube heat exchanger. *Thermal Science and Engineering Progress*, 2, 87-101. England. <https://doi.org/10.1016/j.tsep.2017.05.003>
- [16] Shahril, S. M., Quadir, G. A., Amin, N. A. M., & Badruddin, I. A. (2017). Thermo hydraulic performance analysis of a shell-and-double concentric tube heat exchanger using CFD. *International Journal of Heat and Mass Transfer*, 105, 781-798. England. <https://doi.org/10.1016/j.ijheatmasstransfer.2016.10.021>
- [17] Sharifi, K., Sabeti, M., Rafiei, M., Mohammadi, A. H., & Shirazi, L. (2018). Computational fluid dynamics (CFD) technique to study the effects of helical wire inserts on heat transfer and pressure drop in a double pipe heat exchanger. *Applied Thermal Engineering*, 128, 898-910. England. <https://doi.org/10.1016/j.applthermaleng.2017.08.146>
- [18] Sheikholeslami, M., Gorji-Bandpy, M., & Ganji, D. D. (2015). Fluid flow and heat transfer in an air-to-water double-pipe heat exchanger. *The European physical journal plus*, 130, 1-12. Italy. <https://doi.org/10.1140/epjp/i2015-15225-y>
- [19] Tan, X. H., Zhu, D. S., Zhou, G. Y., & Zeng, L. D. (2012). Experimental and numerical study of convective heat transfer and fluid flow in twisted oval tubes. *International Journal of Heat and Mass Transfer*, 55(17-18), 4701-4710. England. <https://doi.org/10.1016/j.ijheatmasstransfer.2012.04.030>
- [20] Tharakeshwar, T. K., Seetharamu, K. N., & Prasad, B. D. (2017). Multi-objective optimization using bat algorithm for shell and tube heat exchangers. *Applied Thermal Engineering*, 110, 1029-1038. England. <https://doi.org/10.1016/j.applthermaleng.2016.09.031>
- [21] Wickramaarachchi, W. A. M. K. P., & Narayana, M. (2020). Pyrolysis of single biomass particle using three-dimensional Computational Fluid Dynamics modelling. *Renewable Energy*, 146, 1153-1165. England. <https://doi.org/10.1016/j.renene.2019.07.001>
- [22] Xie, C. Y., Tao, H. Z., Li, W., & Cheng, J. J. (2019). Numerical simulation and experimental investigation of heat pipe heat exchanger applied in residual heat removal system. *Annals of Nuclear Energy*, 133, 568-579. USA. <https://doi.org/10.1016/j.anucene.2019.07.009>
- [23] Zhang, H., Yang, J., Zhuang, J., (2009), *Energy saving technology of heat pipe*, China, Beijing: Chemical Industry Press. (In Chinese)